Bulletin of Volcanology (2022) 84: 3
https://doi.org/10.1007/s00445-021-01519-3

RESEARCH ARTICLE

A novel method for the quantitative morphometric characterization of soluble salts on volcanic ash

Ana S. Casas[1] · Adrian Hornby[2] · Carina Poetsch[3] · Corrado Cimarelli[1] · Donald B. Dingwell[1]

Received: 25 May 2021 / Accepted: 16 November 2021 / Published online: 6 December 2021

Abstract

Formation of soluble sulfate and halide salts on volcanic ash particles via syn-eruptive interactions between ash surfaces and magmatic gases is a ubiquitous phenomenon in explosive eruptions. Surficial salts may be rapidly mobilized into their depositional environment undermining the quality of drinking water, harming aquatic life, and damaging soil and vegetation. Assessment of the potential for salt formation on ash and related environmental impacts have been based almost exclusively on bulk mineralogical or chemical analyses of ash; similarly, quantification of surficial salts has been made via leachate analysis only. However, it is the ash surface state and salt crystal properties that exert the predominant control on its reactivity, thus in determining their immediate environmental impact. Here, using scanning electron microscope (SEM) images, we present a novel image analysis protocol for the quantitative characterization of surficial salts, together with chemical analyses of resulting leachates. As volcanic ash proxies, we used synthetic rhyolitic glass particles (with systematic variations in FeO_T and CaO content) and a crushed obsidian. Using an ash-gas reactor, we artificially surface-loaded samples with $CaSO_4$ and NaCl crystals, the most common crystal phases found on volcanic ash surfaces. Analogous variations were found using both methods: for $CaSO_4$ crystals, higher temperature treatments or increasing FeO_T content at the same temperature led to higher concentrations of salt leachate and higher salt volumes; unexpectedly, increasing the CaO content caused only a minor increase in salt formation. In addition to bulk salt formation, morphometric results provided insight into formation processes, nucleation and growth rates, and limiting factors for salt formation. Higher temperatures increased $CaSO_4$ crystal size and surface coverage which we infer to result from higher element mobility in the glasses driving crystal growth. Increasing FeO_T content of the glasses yielded increased salt surface coverage and leachate concentrations, but decreased crystal size (i.e., the salt number density increased). This latter effect likely relates to the role of iron as an electron-donor to charge balance salt-forming cation migration to the ash surface, indicating the importance of iron in determining surface reaction site density and, consequently, environmental reactivity. The controlling roles of ash composition and temperature on salt formation observed here can improve estimations for surface salt formation, volatile scavenging, and environmental impact for eruptions producing glass-rich ash. Our characterization protocol can therefore become a useful tool for the investigation of solid–gas reactions for terrestrial and planetary processes, and it also appears to be a powerful complement to research into atmospheric processes mediated by ash surfaces, such as ash aggregation and nucleation of water or ice on ash.

Keywords SEM imaging · Volcanic ash · Surficial salts · ImageJ · Rhyolite · Solid–gas interactions

This paper constitutes part of a topical collection:

What pyroclasts can tell us

Editorial responsibility: T.P. Fischer

✉ Ana S. Casas
anasilvia.casas@min.uni-muenchen.de

[1] Department of Earth and Environmental Sciences, Ludwig-Maximilians-Universität München, Theresienstrasse 41/III, 80333 Munich, Germany

[2] Department of Earth and Atmospheric Sciences, Cornell University, 112 Hollister Drive, Ithaca, NY, USA

[3] Institute of Earth and Environmental Sciences—Geology, Albert-Ludwigs-Universität Freiburg, Albertstrasse 23-B, 79104 Freiburg im Breisgau, Germany

Introduction

Chemical and physical characterization of volcanic ash (pyroclasts of ≤ 2 mm) has long provided volcanologists with data, which upon careful interpretation, can give insights into the conditions of a given eruption, such as magma composition, duration of the episode, and gas chemistry (Le Maitre et al. 2002; Armienta et al. 1998; Rose 1977). In particular, the chemical analysis of ash leachates (fluid obtained by the dissolution of soluble material from ash surfaces) has been useful to estimate the composition of volatiles in the gas phase of eruptive plumes (Rose et al. 1973). This is because, during explosive eruptions, silicate ash and a hot mixture of gases (mainly H_2O, CO_2, SO_2, HCl, and HF) are turbulently ejected above the magma-fragmentation level, where solid–gas interactions result in formation of sulfate- and halide-bearing salts on ash surfaces (Taylor and Stoiber 1973), the salt-composition can therefore be expected to represent the gas chemistry of an eruptive plume.

The chemical nature and abundance of surficial salts will depend on numerous factors, i.e., style, intensity and duration of the eruption, the grain size distribution of ash, the thermodynamic plume conditions, and gas-mixture composition (many of which cannot be directly observed), yet detailed characterization of surficial salts could help unravel, to some extent, the ash-processing conditions. For example, chemical examination of volcanic ash from the 1970 Hekla eruption (Iceland) combined with high-temperature experiments performed by Óskarsson (1980) suggested that both formation and speciation of fluoride-bearing salts were temperature dependent within the eruption plume column.

Furthermore, recent studies have combined experimental and modeling work to assess the effect of more parameters on salt formation, by using glass particles as a proxy for ash and focusing on high-temperature regimes ($T > 600$ °C), which is highly relevant at in-plume environments (Sparks 1986). For instance, Ayris et al. (2013) tested the potential of glass particles of various magma compositions to react with and uptake (or "sequestrate") SO_2 gas, by means of sulfate-salts formation on the surface of fine-grained particles. Casas et al. (2019) focused on interactions between rhyolitic glass particles and SO_2, further testing the effect of the grain size distribution of glass particles (< 63, 63–90, > 90 μm) and of humidity on formation of surficial salts, by adding 0.01–96 mol.% H_2O to the SO_2-Ar gas mixture. Despite the different experimental procedures used in both studies, their results on high-temperature SO_2 uptake by glass showed compelling similarities: (1) high-temperature uptake of SO_2 predominantly occurred by nucleation and growth of $CaSO_4$ salts on glass surfaces, (2) this occurs more efficiently at $T = 800$ °C, and (3) formation of minor Na- and K-bearing sulfates appears to almost completely cease at $T > 600$ °C.

These results are encouraging, as they not only suggest there is a controlling mechanism by which SO_2 gas reacts with glass surfaces to form surficial salts, but that the process is clearly temperature dependent. Further characterization of glass particles after SO_2 exposure performed by Casas et al. (2019) revealed that the bulk redox state of iron in the glass was changing with temperatures, such that higher iron oxidation, expressed as the ratio between ferric iron and total iron (Fe^{3+}/Fe_T), was obtained at higher temperatures. This finding implied that iron redox processes might be linked to SO_2 uptake processes (thus, $CaSO_4$ formation), which could become critical for investigation of salt formation on iron-rich ash. These studies clearly demonstrated the feasibility of reproducing, to some extent, the natural formation of surficial salts on volcanic ash proxies, and stressed the fact that more detailed salt characterization can be useful to better constrain salt formation mechanisms. This is of interest due to the fact that interactions between ash and receiving environments occur in great measure by means of surface-mediated processes, such that the surface composition of ash (including surficial slats) will exert a significant control in determining ash reactivity upon contact with the biosphere (Ayris and Delmelle 2012). Furthermore, syn-eruptive formation of slats and subsequent deposition of salt-loaded ash onto receiving environments are key steps of the recycling of elements on earth (Rose 1977).

We herein aim to contribute to the improvement of characterization of surficial salts on ash proxies. For this, we used natural and synthetic glasses—the latter designed to test the effect of varying iron and calcium content in glass on surficial salt formation—that were artificially loaded with the most common salts found in volcanic ash ($CaSO_4$, NaCl). We did so, by reacting glass particles with customized gas mixtures (1 mol.% of SO_2 or HCl in Ar) at various high temperatures (600–900 °C) and exposure times (0.5–4 h), using the Advanced Gas-Ash Reactor (Ayris et al. 2015). We then acquired leached data and SEM images for all samples. Next, we developed a semi-automated macro-based method with the image-processing program ImageJ (Schneider et al. 2012) that allowed us to determine diverse size and shape properties from SEM images of the surficial salts formed on glass particles and estimate the total surficial area occupied by salts on the surface of the particles. Thereafter, we compared the image-based quantification with corresponding leachate data to evaluate the robustness and accuracy of this method for bulk evaluation of surficial salt loading on the particles used here. Finally, we described the results and the implications and limitations of our method and stressed some considerations required for reliable extrapolation for volcanic ash.

Methods

Sample preparation

As a reproducible and well-characterized proxy for volcanic ash particles, we have prepared a set of starting powdered materials from natural and synthetic rhyolitic glasses. Using the AGAR reactor (Ayris et al. 2015), an apparatus capable to generate ideal conditions for high-temperature solid–gas reactions, the glass powders/ash analogs were artificially loaded with sulfate and chloride salts, mostly $CaSO_4$ and NaCl. We chose glass particles to simulate ash due to (1) the ubiquity of glass in ash componentry (Heiken 1972, 1974; Heiken and Wohletz 1985; Wilson and Stewart 2012) and (2) the fact that previous studies have experimentally shown that glass is highly reactive towards SO_2 and HCl at high temperatures and is, therefore, a suitable ash proxy for ash-gas experiments (Ayris et al. 2013, 2014). Furthermore, we focused on rhyolites, after Casas et al. (2019) noticed a higher reactivity of these towards SO_2 than previously reported by Ayris et al. 2013; such that after exposing rhyolite glass particles to 1 mol.% SO_2 at 800 °C for 1 h, Casas et al. (2019) reported incorporation of ~ 80% of the calcium in the glass to form surficial anhydrite deposits ($CaSO_4$); in contrast, Ayris et al. (2013) reported only ~ 34% under similar experimental conditions.

Thus, assuming that the variations in composition between the two rhyolites, in particular the calcium oxide (wt.% CaO) and total iron (wt.% FeO_T), were responsible for the observed discrepancies in SO_2-rhyolite reactivity, we here tested a wider range of rhyolitic compositions for the experimental material: (1) natural rhyolite, collected from the sampling site "AO" (Tuffen and Castro 2009) of the obsidian ridge Hrafntinnuhryggur (Krafla volcanic system, Iceland) and (2) two sets of haplogranitic glasses (a widely used analog material for rhyolites), based on the composition designated as HPG8 by Holtz et al. (1992), that we here further doped with 1 and 2 wt.% of CaO and 0, 1, and 2.5 wt.% FeO_T. The bulk chemical composition of all materials is reported in Table 1. HPG8 glasses were prepared by mixing the following ChemPUR® analytical reagent-grade oxides and carbonates: SiO_2, Al_2O_3, K_2CO_3, Na_2CO_3, $CaCO_3$, and Fe_2O_3. All oxides were pre-dried overnight at 120 °C, before mixing. Each oxide mixture was melted under atmospheric conditions in a Nabertherm® electrical resistance $MoSi_2$ box furnace at 1550 °C and then transferred to a viscometry

Table 1 Bulk chemical composition (in wt.%) of HPG8 glasses and natural rhyolite. An average of 30 measurements per sample were acquired

Sample	HPG8 CaO 1			HPG8 CaO 2			Krafla rhyolite
	+1 wt.% CaO			+2 wt.% CaO			
	+0 wt.% FeO_T	+1 wt.% FeO_T	+2.5 wt.% FeO_T	+0 wt.% FeO_T	+1 wt.% FeO_T	+2.5 wt.% FeO_T	
SiO_2	78.28	78.19	77.08	76.34	75.38	74.36	75.95
St dev	0.36	0.34	0.31	0.64	0.55	0.79	0.61
TiO_2	0.02	0.02	0.03	0.03	0.04	0.04	0.23
St. dev	0.02	0.02	0.03	0.03	0.03	0.04	0.03
Al_2O_3	11.76	11.66	11.35	11.78	11.44	11.44	11.91
St. dev	0.13	0.25	0.13	0.22	0.11	0.07	0.12
FeO_T	0.09	1.04	2.59	0.04	1.02	2.45	3.26
St. dev	0.06	0.06	0.16	0.02	0.02	0.08	0.08
MgO	0.02	0.02	0.01	0.01	0.01	0.02	0.09
St. dev	0.01	0.01	0.01	0.01	0.01	0.01	0.01
CaO	1.14	1.12	1.14	2.19	2.14	2.15	1.7
St. dev	0.06	0.03	0.04	0.06	0.05	0.05	0.04
Na_2O	4.58	4.43	4.1	4.43	4.36	4.2	3.74
St. dev	0.11	0.11	0.1	0.1	0.06	0.1	0.5
K_2O	4.07	4.01	3.96	4.22	3.99	3.95	2.65
St. dev	0.06	0.05	0.04	0.05	0.06	0.06	0.04
SO_2	0.01	0.01	0.01	0.01	0.01	0.01	0.01
St. dev	0.01	0.01	0.01	0.01	0.01	0.01	0.01
P_2O_5	0.04	0.04	0.03	0.04	0.05	0.02	0.02
St. dev	0.02	0.02	0.01	0.02	0.02	0.02	0.01
Total	100.01	100.54	100.3	99.09	98.44	98.64	99.56

furnace where they were stirred to equilibration and finally rapidly quenched by immersion in distilled water. Next, the HPG8 glasses and the Krafla rhyolite were dry-milled using a Retsch GmbH® S1000 zirconium dioxide centrifugal ball mill, then sieved to achieve a grain size distribution of 63–90 μm, representative of fine ash (Ayris and Delmelle 2012), and finally stored in glass vials until experiments were performed (see Supplementary Figs. 1 and 2).

Experimental treatment and characterization of samples

Artificial loading of sulfate and chloride salts on glass particles involved exposing ~ 2 g of each sample to a flow of 25 standard cubic centimeters per minute (sccm) of the gas mixtures SO_2 or HCl (both 1 mol.% in 99 mol.% Ar) at 600, 700, 800, and 900 °C, each time for 0.5, 1, or 4 h long. This salt-loading procedure has been previously described by Casas et al. (2019) for the Krafla rhyolite and was replicated here to treat the HPG8 glasses. Doping the latter with CaO and FeO_T allowed us to test the influence of glass composition on surficial salt formation. Both the Krafla rhyolite and the HPG8 glasses were exposed to the SO_2-Ar gas mixture, while only the Krafla rhyolite was also treated with the HCl-Ar mixture—this is due to previous observations of lower reactivity of rhyolites towards HCl, when compared to SO_2 (Casas et al. 2019). The exposure temperatures (600–900 °C) were chosen after precedent studies have implied that temperatures near or at the glass transition (Tg) enhance the occurrence of gas-ash reactions, thus surficial salt formation (Delmelle et al. 2018; Renggli and King 2018).

Moreover, the temperature regimes at the environments where ash-gas reactions take place, e.g., in-conduit, in-plume, or in-PDCs, are within this range (Castro and Dingwell 2009; Sparks 1986; Paterson et al. 2010; Banks and Hoblitt 1981). After each experiment, salt-loaded glass powders were rapidly removed from the reactor, left to cool at ambient temperature, and stored in sealed glass vials until characterization. Electron imaging and bulk chemical analysis of pristine and treated samples were obtained using a Hitachi® SU-5000 Schottky field emission scanning electron microscope (FE-SEM). To determine the bulk chemistry of surficial salts, separate aliquots of pristine and treated samples were leached at room temperature with deionized water for 1 h, at a 1:250 solid:water ratio and vacuum-filtered through a MF-Millipore® 0.22 μm mixed cellulose ester membrane. The filtered leachates were then analyzed with a Metrohm® ion chromatography system. Soluble cations (Ca^{2+}, Mg^{2+}, K^+, and Na^+) and anions (SO_4^{2-} and Cl^-) were analyzed using the separation columns Metrosep C4-150/4.0 and Metrosep A Supp 5–150/4.0, respectively. Bulk iron redox state measurements were performed using the method described by Shapiro and Brannock (1956). Prior to the experiments, the specific surface area ($m^2\ g^{-1}$) of powdered samples was measured with the Brunauer, Emmett, and Teller (BET) method (Brunauer et al. 1938), using a 9-point He-adsorption isotherm acquired with a Micromeritics Gemini III 2375 surface area analyzer (Supplementary Table 1).

Image analysis and macro structure

Secondary electron images of each salt-loaded sample captured at a range of magnifications (5000 to 40,000 ×) show the shape and size of multiple surficial salts. Each 2560 × 1920-pixel image was composed of a greyscale that discriminates the salt crystals formed during gas-glass reactions, shown with a light-grey color, from adhering glass fragments, shown with lighter-to-darker grey colors. The objective of the image analysis was first to classify the images into glass background, surface salts, and adhering (non-salt) particles and then measure the morphometrics and the total area fraction of the salts for each image. We selected the most suitable images for analysis from each experimental condition (i.e., clear greyscale contrast, flat surface, and consistent background shade) and saved them as.tif files. The pixel dimension of images varied from a minimum of ~ 1.5 to ~ 110 nm^2, but higher magnification images were chosen whenever possible. We imposed a lower limit of 5 pixels for any feature, and the smallest salts we measured were ~ 10 nm^2. Greyscale smoothing and thresholding operations minimized the chance of misidentification of the smallest salt crystals.

Images were analyzed using a sequence of semi-automated macros created in the open-source image analysis software ImageJ (https://fiji.sc/) and written in the native IJ1 language. An overview of the workflow for the macros is given in Fig. 1. Image processing steps were made with the ImageJ native functions, except for background noise reduction using the Non-linear means denoising plugin (Darbon et al. 2008), opening, closing, and dilation operations, which were conducted using the MorphoLibJ plugin (Legland et al. 2016) (https://imagej.net/MorphoLibJ) and the Disconnect particles plugin (Münch et al. 2006). Particle measurements were made using the Shape Filter plugin (Wagner and Lipinski 2013) (https://imagej.net/Shape_Filter). Finally, we used a custom setup of the Read and Write Excel plugin (https://imagej.net/User:ResultsToExcel) to collate and rearrange shape results in a batch process into separate tabs in Microsoft Excel to ease analysis. The macro either operates on single images or runs sequentially through images within a folder (batch mode). Output files are saved in separate folders for each image, using the image file name as title, allowing analysis steps to be repeated and checked and standalone submacros to be run on the output files. The master macro (Salts_AGAR.txt) described in Fig. 1 is available, together

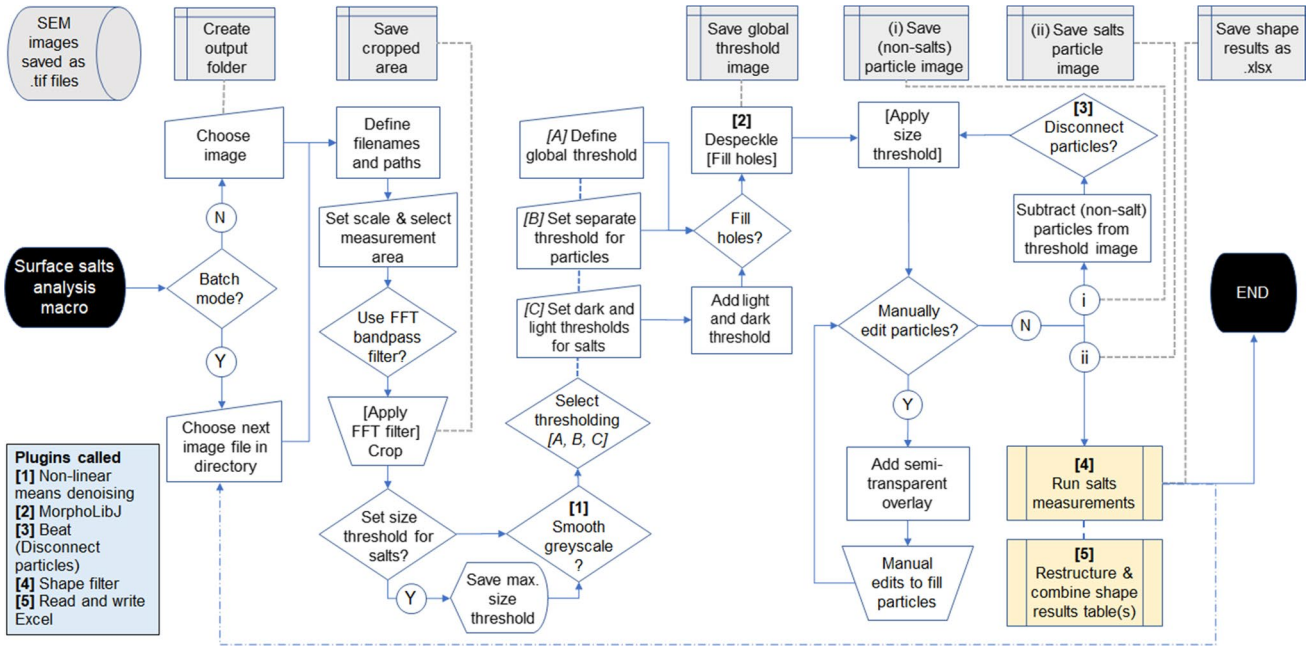

Fig. 1 Flowchart describing the ImageJ macro procedure used to segment salt crystals from SEM-SE imagery of glassy particle surfaces. Blue solid arrows show linked steps and grey dashed lines indicate where files are saved. Dashed blue lines show optional paths. Box shapes are described in the key and ImageJ plugins (numbered 1–5 in the flowchart where they are called) are shown in the blue legend. See text for links and references to the plugins

with modular submacros for standalone salt morphometric analysis (salts_shape_filter.txt) and shape results table rearrangement (shape_results_arrangement_AGAR.txt) at https://github.com/hornbya/Ash-surface-salts.

The macro operates by segmenting all surface components from the background (a global threshold), before further segmentation of adhering (non-salt) particles from salt crystals, via a user-determined combination of (a) a visual, user-defined size threshold, assuming the salts are smaller than the particles; (b) greyscale thresholding options; and (c) manual correction using a semi-transparent greyscale image overlay as a guide and run as a loop to aid non-salt particle selection. The classified non-salt particles are subtracted from the global threshold, to produce a salts-only classified image. A final manual correction loop is run on the segmented salt image. Finally, overlapping particles are defined and separated by a watershed. Salt crystals are then analyzed for size, shape, and area fraction, using measurements calculated from the Shape Filter plugin, which improves perimeter estimation compared to the native Analyze Particles function. Shape factors and the results table reorganization macro were defined following previous work (Liu et al. 2015; Guimarães et al., 2019; Hornby et al. 2020).

The impact of choices and judgment during macro analysis by different users was partly evaluated and mitigated by comparing and combining image analysis results obtained independently by AH and CP. For three identical images that were analyzed separately by both operators, salt coverage varied by 2.5–7.5%. For 14 experiments, results from both operators were used to provide average values for bulk (salt coverage) and single-particle (morphometrics) measurements. The projected area of salt crystals was used as the basis for salt volume estimation. We used a simple cuboid model, wherein the principal axes x, y, and z were related by $x = y = 2z$ and xy = measured particle area. This ratio was chosen to best match the apparent salt shapes present across a survey of the SEM images (Fig. 2); however, it clearly does not suit the apparent crystal shapes in some instances, particularly for iron-free and low-temperature experiments; in these cases, the cuboid model likely leads to a significant overestimation of the volume. Salt crystals produced here take a variety of forms, and further work to constrain the z-axis dimension directly from SEM imagery will be a useful improvement for subsequent studies.

Results

Raw SEM images

Surficial salts were observed for all samples after SO_2 and HCl exposures. Figure 2 shows surficial salts formed after SO_2 treatment on HPG8 glasses (panels a–r) and Krafla rhyolite (panels s–u), while HCl-treated samples (only Krafla

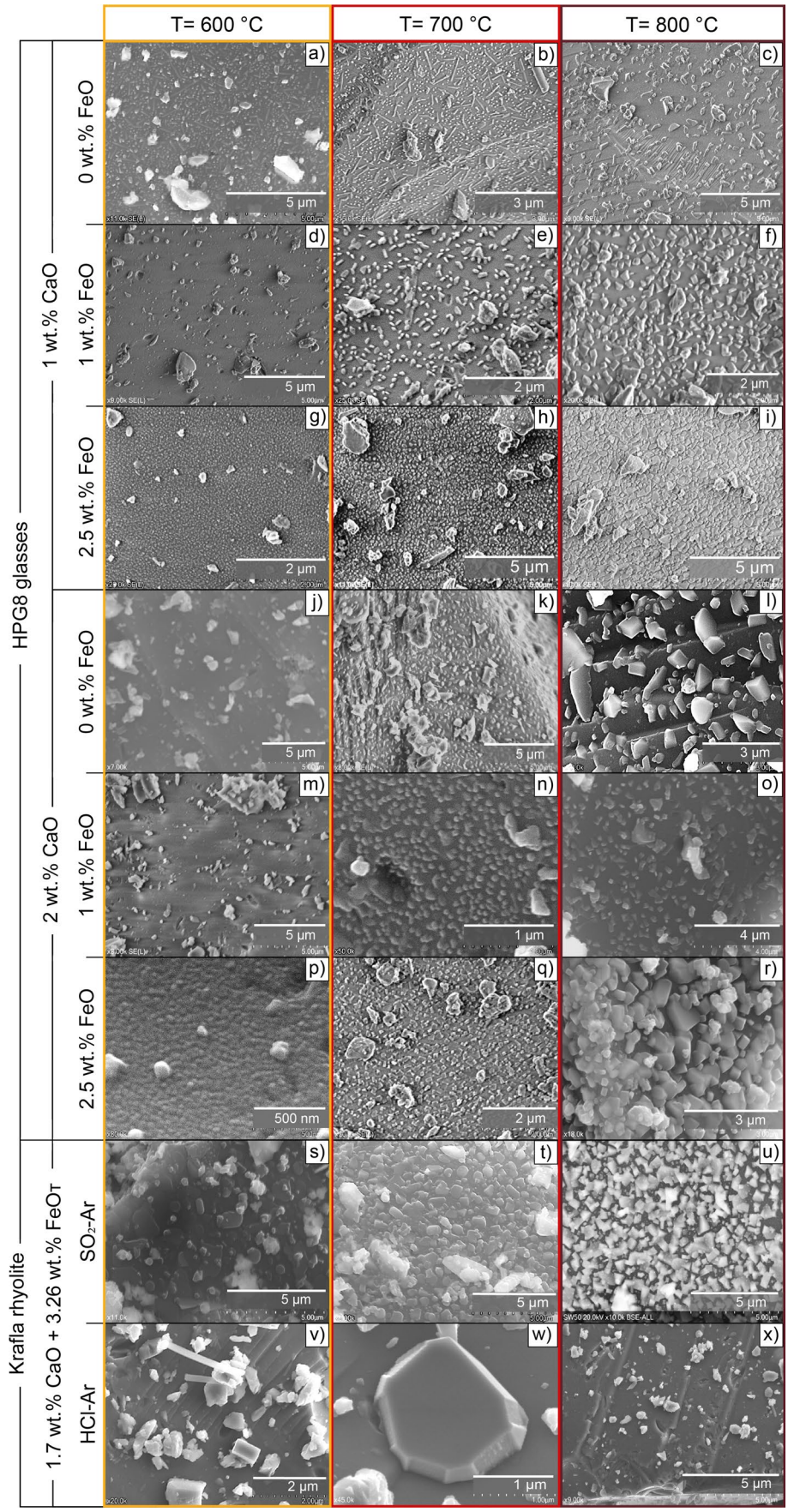

Fig. 2 SEM images of products formed on surfaces of HPG8 CaO 1 (**a–i**), CaO 2 (**j–r**), both treated with SO_2 only, and Krafla particles exposed to SO_2-Ar (**s–u**) and HCl-Ar **(v–x)**. The outline color of the images yellow, red, and dark red represents the treatment temperatures, 600, 700, and 800 °C, respectively

rhyolite) are seen in panels v–x. The images of SO_2-treated samples display two main distinctive features: (1) the largest and more abundant distributed salts are consistently seen at $T = 800$ °C and (2) the chemical composition of the glasses appears to strongly influence the morphology of the surficial salts. This becomes particularly evident for the treated HPG8 samples (Fig. 2a–r), where salts formed on Fe-free samples (HPG8 0 wt.% FeO_T) doped with 1 and 2 wt.% CaO (Fig. 2a–c and j–l, respectively) seem to be smaller (< 0.5 μm) and display more variable aspect ratio, when compared to those formed on Fe-bearing samples (see Fig. 2d–i and m–r). Surficial salts formed on Krafla rhyolite particles after SO_2-exposure (Fig. 2s–u), appear to be generally larger (≤ 1 μm), and have a higher surface coverage than those observed for the HPG8 set of samples. For surficial salts formed during HCl treatments (Fig. 2v–x), both angular (cubic and rectangular) and elongated cylindrical shapes, as long as 2 μm (Fig. 2v), can be observed, in contrast to the surficial salts resulting from SO_2 exposure, that were predominantly angular and blocky. For samples treated with HCl-Ar, the effect of temperature on salt formation seems to be opposite to that observed for SO_2 treatments, namely, that the size and abundance of surficial salts consistently decrease with increasing temperatures.

Leachate analysis

Results of leachate analyses of SO_2-treated samples showed calcium (Ca^+) to be the main cation released upon dissociation of surficial salts. Minor amounts of sodium (Na^+) and potassium (K^+) were also detected (see Supplementary Fig. 3) but are negligible in all cases, when compared to calcium concentrations. In HCl-treated samples, both Ca^+ and Na^+ were found to be present at the surface as $CaCl_2$ and NaCl, respectively. Figure 3 shows the effect of gas and glass composition, temperature, and exposure time on the formation of surficial salts, evaluated by leachate concentrations. For SO_2-treated samples, the enhanced salt formation on particle surfaces upon increasing temperatures observed in Fig. 2 is consistent with the higher concentrations of leached calcium, as the highest concentrations of leached Ca^{2+} were obtained at $T = 800$ °C. Increasing exposure times also led to increased leachate concentrations (Fig. 3c). Conversely, in the case of HCl-treated samples, increasing temperatures led to lower Ca^{2+} concentrations, in agreement with images shown in Fig. 2v–x.

SEM image analysis

Segmentation and morphometric analysis of surface phases from high-magnification SEM-SE-images enabled quantitative characterization of surface salts on a single-particle basis. A total of sixty-eight high-magnification SEM-SE-sample-images were chosen for analysis. Images without clear focus or with significant streaking or lighting variations were rejected to allow for a higher quality morphological characterization of the rest. Where possible, results from multiple non-overlapping images for a single sample were combined, covering twenty-six samples with the number of individual salt crystals measured varying between 105 and 8547 per sample, with a median of 1050. Shape and size results were plotted as boxplots, showing the mean, median,

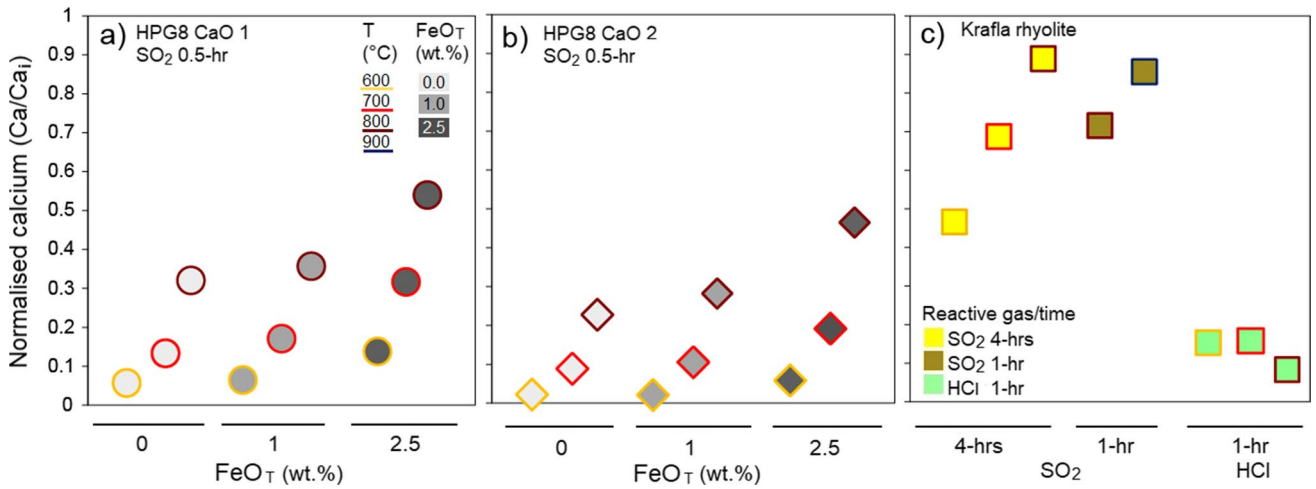

Fig. 3 Normalized leached calcium concentration (Ca/Ca_i) of HPG8 and Krafla rhyolite treated samples. Normalized calcium was calculated by dividing the concentration of leached calcium from each sample (Ca^{2+}) by the initial bulk concentration of calcium (Ca_i) of the initial material, i.e., 8076, 1537, and 12,149 mg kg^{-1} calcium in the HPG8 CaO 1, CaO 2 and Krafla rhyolite samples, respectively. Data points of HPG8 samples doped with 1 and 2 wt.% CaO are plotted in panels **a** and **b**. The gray shades represent the amount of FeO_T in each sample (see inset), while the border color represents the treatment temperature. Krafla rhyolite data are shown in panel **c**, for each of the three gas mixtures tested (see inset)

interquartile range, and potential outliers for each experiment. Here, we present the results obtained from the image analysis that resulted in quantitative data of salt surface coverage (Fig. 4), salt crystal area (Fig. 5), salt number density (Fig. 8), salt crystal roundness (Fig. 9), median salt crystal volume (Fig. 10), mean salt crystal volume (Fig. 11), and salt surface loading (Fig. 13).

Salt crystal coverage

Salt coverage is defined here as the percentage of analyzed particle surfaces occupied by salt crystals. In Fig. 4, the salt coverage measured by image analysis for all experiments is shown, with error bars representing the standard deviation between multiple images for the same sample. HPG8 and Krafla samples treated with SO_2 show a bulk trend of increasing coverage upon increasing temperature; however, the magnitude of increase varies between different sets of experiments. Within the HPG8 data (Fig. 4a–b), increasing FeO_T content has a comparable effect to temperature in increasing salt coverage. For experiments of HPG8 samples doped with 0 and 1 wt.% FeO_T, we observe no significant change in coverage between 700 and 800 °C,

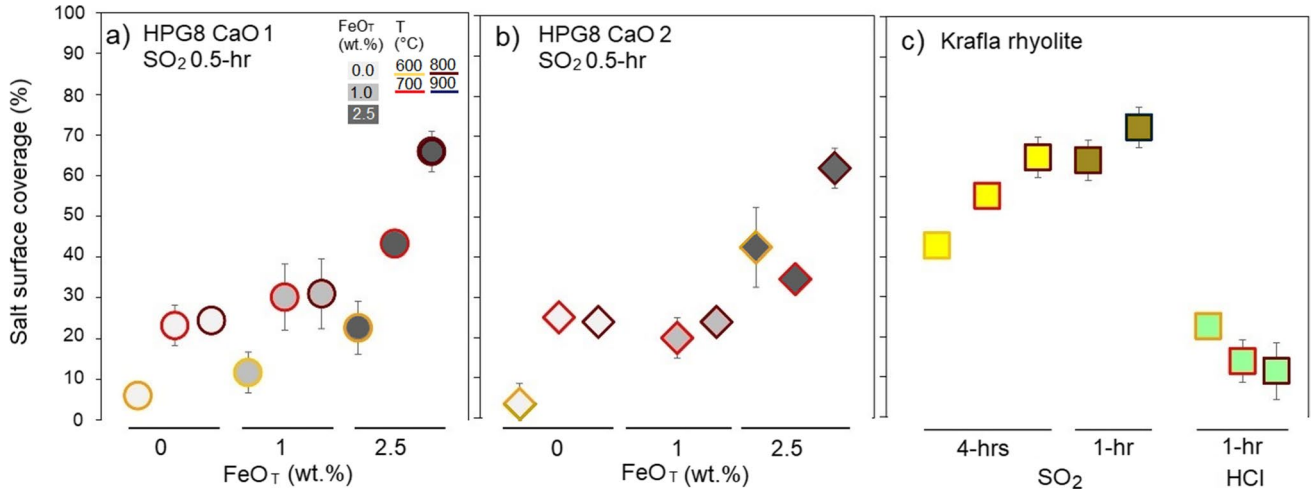

Fig. 4 Average salt surface coverage for all experiments, following the same layout as Fig. 3. Error bars show the standard error between multiple images from the same sample and are smaller than the symbols when not visible. For single images, the error is estimated at ± 5% given the variability in results from different operators. In general, the fraction of particle surface covered by salts increases with temperature, except for experiments with an HCl-atmosphere, where salt coverage reduces with increasing temperature. For the HPG8 experiments, higher FeO_T at a fixed temperature content correlates with increasing salt surface coverage. Reasonable gross correlations can be found with leachate data in Fig. 3

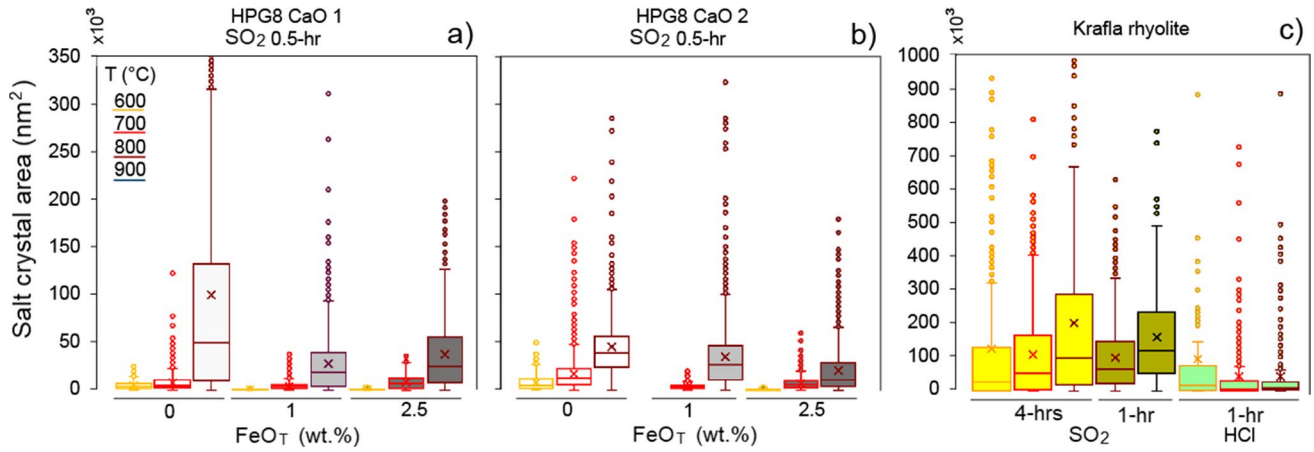

Fig. 5 Median salt area for each experiment, presented as box plots for all experiments. Boxes show the interquartile range (IQR; 25th to 75th percentile of the result), whiskers are 1.5 × the IQR, and data points are potential outliers. The median is shown as a horizontal line and the mean as a × within each box. Box outline and fill colors denote the experimental temperature, seen in the inset below panel **a**

while for samples with 2.5 wt.% FeO_T, salt coverage increased by 20–25% over the same temperature step.

Increasing CaO content from 1 to 2 wt.% had little effect on salt coverage. The 4-h Krafla experiments (Fig. 4c) under SO_2 treatments showed incremental increase of ~ 15% salt coverage for each 100 °C rise in temperature. The increase in coverage between 1- and 4-h experiments (Krafla rhyolite at 800 °C) is observed to be just a few percent. For HPG8 samples, maximum salt surface coverages were 65 and 62%, corresponding to samples CaO 1 and CaO 2, both doped with 2.5 wt.% FeO_T and treated at 800 °C, while the lowest values of 3.5 and 6 corresponded to samples CaO 2 and CaO 1, which were both Fe-free and treated at 600 °C. For Krafla rhyolite samples treated with SO_2, the maximum surface coverage was obtained by the sample treated at 900 °C for 1 h, 72%, while the lowest coverage, 42% was produced by the sample treated at 600 °C for 4 h. Under HCl treatments, the salt coverage values of Krafla samples were noticeably lower than those produced by SO_2 experiments and showed an inverse correlation with temperature, i.e., higher temperatures produced lower salts coverages, namely, 22, 13, and 11%, corresponding to experiments performed at 600, 700, and 800 °C, respectively, all 1 h long.

Salt crystal area

Salt crystal area was measured directly via image analysis and represents the 2D projection of the outer extremity of each salt crystal; however, given the observed morphology of the salts and near-perpendicular viewing angle for SEM images, the measured salt area is likely to only slightly overestimate the area of a cross-section parallel to the ash particle surface. For HPG8 samples, Fig. 5a–b shows that salt crystal area increased with temperature between 600 and 800 °C. An increase in temperature from 600 to 700 °C had a minor effect on salt crystal size compared to the increase from 700 to 800 °C, which increased average salt crystal area by a factor of 2–8. For a given temperature, salt area was inversely correlated to the FeO_T content, with the largest salts observed for Fe-free samples treated at T = 800 °C, while the smallest salts were formed at 600 °C and 2.5 wt.% FeO_T. We observed no systematic dependence on CaO content, between 1 and 2 wt. %; however, median salt sizes are often smaller—over twice as small in some cases (e.g., at 800 °C). The salt crystal size frequency distributions for HPG8 experiments are reported in Fig. 6. The distributions are usually unimodal, becoming increasingly fine-skewed and broader with increasing experimental temperature and occasionally showing a secondary fine peak (e.g., the distribution for CaO 1 + 1 wt.% FeO_T at 600 °C). For SO_2-treated Krafla samples (Fig. 5c), we observed the same trend, but with a stable increase with temperature, as salt crystal area approximately doubled with each 100 °C temperature rise between 600 and 900 °C.

The effect of experimental duration could be evaluated only for one experiment; at 800 °C, salts were one-third smaller in area after 1 h compared to 4-h experiments. Experiments on Krafla samples in an HCl atmosphere showed a decrease in crystal size between 600 and 700 °C, in contrast to all SO_2 experiments, where crystal sizes increased with temperature. In Fig. 7, we plot salt coverage against median salt crystal area. A general trend of increasing both salt coverage and salt crystal area with FeO_T content and temperature can be seen for all experiments; however, salt crystal size is more sensitive to temperature than FeO_T content for HPG8 samples (Fig. 7a). Lower FeO_T content appears to limit salt coverage, with only the 2.5 wt.% FeO_T samples reaching > 30% coverage; on the other hand, higher FeO_T often correlates with smaller crystal sizes, suggesting higher salt number density. For Fe-free HPG8 samples, we observe a jump in salt coverage at higher temperature, from ~ 5% at 600 °C to ~ 25% at 700 and 800 °C. For samples with 1 wt.% FeO_T, salt coverage clustered at 20–30% for all temperatures, while experiments with 2.5 wt.% FeO_T showed increases of 15–25% for every 100 °C increase in temperature.

Krafla samples (1.7 wt.% CaO and 3.26 wt.% FeO_T) showed a similar dependence on temperature to the 2.5 wt.% FeO_T HPG8 samples, but median crystal sizes were up to an order of magnitude larger (Fig. 7b). Both salt coverage and crystal size decreased between 600 and 700 °C for HCl experiments. Interpretation of salt coverage data can be complemented by information on salt number density and crystal size. We measure salt number density as the total number of salts over the available surface area (i.e., the glass particle area not obscured by adhering non-salt particles). The results in Fig. 8 show salt number density increasing with FeO_T content and decreasing with temperature for HPG8 samples (Fig. 8a). Krafla rhyolite samples have lower salt number density than HPG8 samples but also show slight decreases in number density with temperature above 700 °C (Fig. 8b).

Salt crystal shape and volume estimation

Amongst the sulfur-exposed samples, a wide variety of salt crystal shapes were observed upon changing the glass composition. While treated Krafla samples, displayed a rather constant salt shape, i.e., compact and increasingly angular, for all temperatures, HPG8 samples appeared to have a larger range of shapes, seemingly controlled by FeO_T content and temperature. In Fig. 2a–c, treated Fe-free samples display the strongest variability in crystal shape; at $T = 600$, 700 °C, salts can be observed as small dot-like crystals (diameter ~ 0.1 μm) and needle-like crystals (length ~ 0.5 μm), while at $T = 800$ °C, most crystals

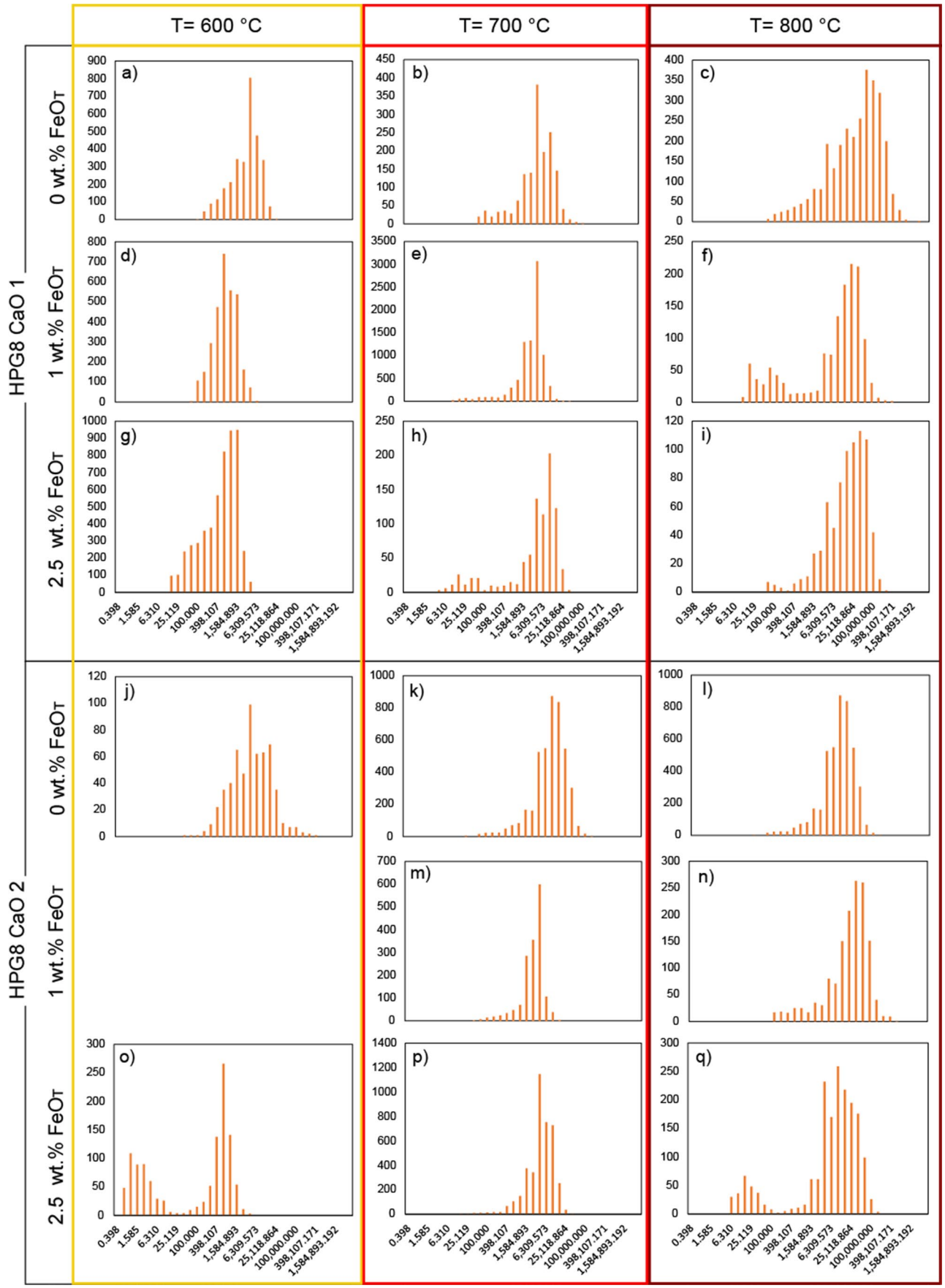
T= 600 °C
T= 700 °C
T= 800 °C
HPG8 CaO 1
HPG8 CaO 2
0 wt.% FeOT
1 wt.% FeOT
2.5 wt.% FeOT
a)
b)
c)
d)
e)
f)
g)
h)
i)
j)
k)
l)
m)
n)
o)
p)
q)
0.398
1.585
6.310
25.119
100.000
398.107
1,584.893
6,309.573
25,118.864
100,000.000
398,107.171
1,584,893.192

◂**Fig. 6** Number size distributions of salt crystals for all HPG experiments (CaO 1 in upper nine panels, CaO 2 in lower eight panels). The frequency of salt crystals (x-axis) in each size bin is represented by the column height. The y-axis represents the particle diameter in nanometers (nm). The sample treatment temperature, 600, 700, and 800 °C is indicated by the border column colors, yellow, red, and dark red, respectively

lack the previously observed shapes and rather appear to have a more uniform angular shape. Results of the image analysis show aspect ratios of 0.55–0.7 for all experiments, with no consistent changes correlated to temperature or composition. However, a trend for decreasing salt crystal roundness (Fig. 9) with increasing temperature is consistently observed for all HPG8 CaO 1 samples and most of HPG8 CaO 2 and Krafla rhyolite samples.

In contrast, experiments on Krafla treated with HCl showed that salt crystals became more rounded with increasing temperature. Direct comparison between the image analysis and leachate results requires constraints on salt volumes. We calculate salt volumes on a single-particle basis using a simple cuboid model, as described in "Methods." We present median salt crystal volume for each experiment in Fig. 10. Mean values are useful to compare to total salt volumes, but median volume values may be more characteristic of actual salt sizes due to skewing by the largest particles in many samples, as the number distributions in Fig. 6 become highly coarse-skewed volume distributions. We present mean salt volumes in Fig. 11, which show universally greater volumes, but very similar trends to Fig. 10 and an apparent jump in size between HPG8 and Krafla samples. A consistent increase in median salt volume can be seen with temperature for all SO_2 experiments, with crystals averaging $> 10^7$ nm^3, or 0.01 μm^3 each in volume, produced during SO_2 experiments at 800 °C, for 1–2 h duration on Krafla obsidian (Fig. 10b).

The smallest salts, produced during 0.5-h experiments at 600 °C on HPG8 samples with 2.5 wt.% FeO_T, have median volumes $< 10^4$ nm^3. We observe that median volume decreases for samples with 0 wt.% and 1 wt.% FeO_T content for HPG8 samples in Fig. 10a, while size remains constant between 700 and 800 °C. In Fig. 12, we further plot the median salt crystal volume against the salt number density (i.e., the total number of salts over the available surface area) and observe a strong correlation between both parameters, as greater salt volumes are associated with reduced salt number densities. This seems to further correlate well with increasing temperature for both HPG8 and Krafla samples, with the exception of Fe-free HPG8 samples. All SO_2-treated samples can be fitted with a linear regression (taking the form of a power law where $y = 0.035x^{-1.36}$ with an R^2 of 0.77, calculated using a robust Cauchy fit), while HCl-treated samples seem not only to deviate from it, but also behave inversely upon temperature increase.

Discussion

Our results show that the SEM image analysis protocol presented here was successful in performing quantitative characterization of salt morphology and salt surface coverage of fine-sized particles. Despite the limitations of resolution and contrast on processing images of submicron-sized surficial salts (see "Methods"), a good agreement was observed between leached calcium concentration data (i.e., a measure of the bulk amount of total salts formed on the particles) for the experimental parameters tested (gas mixture, temperature, exposure time, and glass composition) and the salt surface coverage (%) and salt loading obtained from SEM image analyses. The crystal size, chemical nature, and morphology of salts presumably determine their reactivity in natural environments, considering that the surface area to volume ratio of the salts can be expected to determine the dissolution rate. Here, both the salt-loading procedure and experimental settings were carefully designed to best replicate the natural conditions of syn-eruptive salt growth during ash-gas interactions, e.g., the experimental temperatures were chosen to comprise a characteristic range of potential reaction environments, i.e., in-conduit, in-plume, or in-PDCs (Banks and Hoblitt 1981; Castro and Dingwell 2009; Sparks 1986; Paterson et al. 2010); the concentrations of 1 mol.% of both SO_2 and HCl in the gas mixture fall within reported average values of both gases in volcanic emissions (Textor et al. 2003); the reaction times, 0.5–4 h, can be expected to correspond to large- to very-large (VEI ≥ 6) eruptive events time-frames (Rampino and Self 1982; Pyle 2000); the grain size distribution is within the definition of fine ash (Rose and Durant 2009); and the glass compositions are representative of natural rhyolites (Rogers and Hawkesworth 2000).

Furthermore, both the chemical composition of the salts produced during SO_2 and HCl experiments, $CaSO_4$ and NaCl, respectively, as well as their concentrations, in milligrams of the species per kilogram of the sample (mg kg^{-1}), are within the mean values of previous reports of volcanic ash analysis (see Supplementary Table 2). Nonetheless, we acknowledge that our controlled experiments greatly simplify the number of eruption parameters and their combined effects on ash-gas reactions (thus, salt growth), e.g., the presence and speciation of other volatiles in the exolved gas mixture (e.g., HF, H_2SO_4, and CO_2), air entrainment, plume dilution, temperature variations, and turbulent ash-gas flow, which were not possible to test here, due to the technical limitations of the apparatus

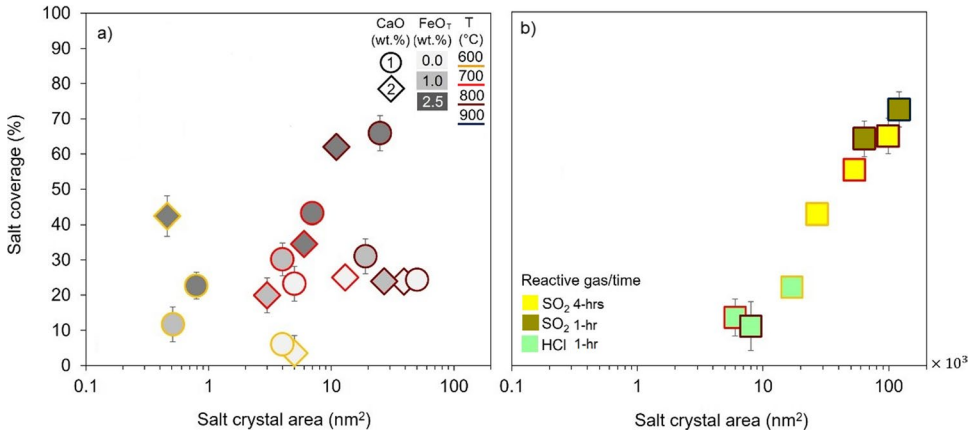

Fig. 7 Salt surface coverage with varying FeO_T content. **a** HPG8 data is shown as grey circles (1 wt.% CaO) and rhombi (2 wt.% CaO). **b** Data of SO_2-treated Krafla samples is shown as squares for the 1- (dark yellow) and 4-h (yellow) experiments, while data for samples treated with HCl-atmosphere are shown as green squares

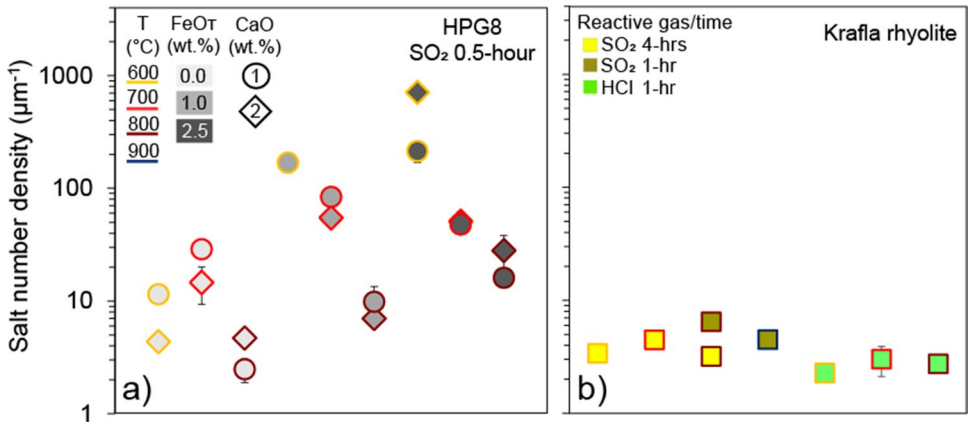

Fig. 8 Salt number density for **a** HPG8 and **b** Krafla rhyolite experiments. The y-axis in panel **a** applies to both panels

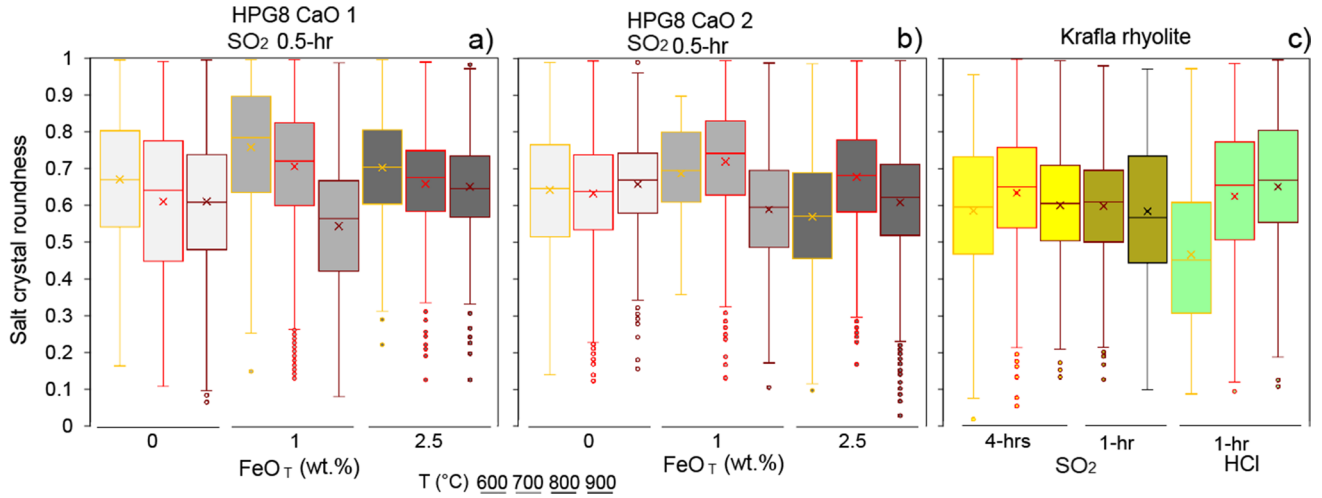

Fig. 9 Salt crystal roundness boxplots, with sample type, reactive gas, and experiment duration in the title above each panel, and experimental conditions described by boxplot color and border color and stated in the key for each panel. Note that salts become slightly rounder with increasing temperature for all experiments in an SO_2 atmosphere, with the opposite being true for HCl experiments

(Ayris et al. 2015). We chose not to test the effect of water vapor on surficial salt formation, as this was thoroughly investigated by Casas et al. (2019). The authors tested the effect of adding water vapor (0.01–96.41 mol.% H_2O) to both SO_2 and HCl mixtures (1 mol.% of each in Ar) and found that above $T > 600$ °C and even at supersaturated

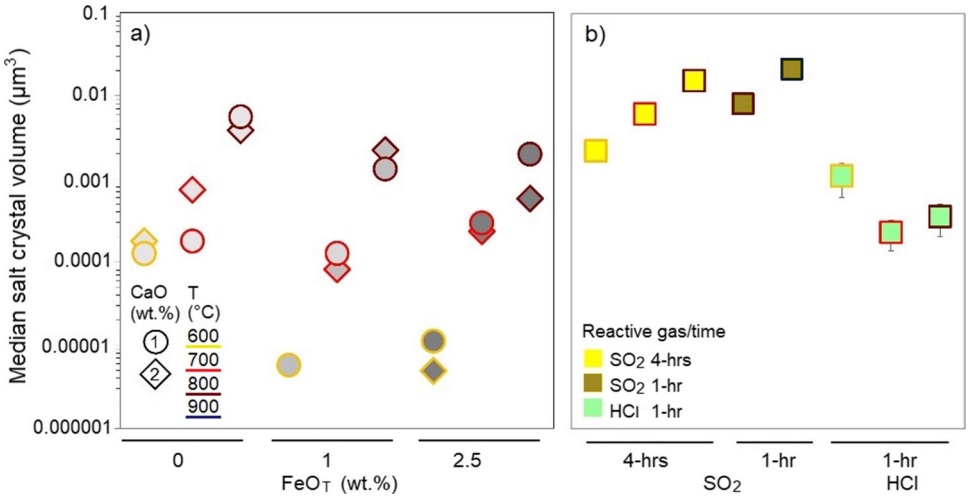

Fig. 10 Median salt crystal volume (μm^3) for each experimental treatment of **a** HPG8 glasses and **b** Krafla rhyolite. Error bars show the median absolute error and are smaller than the symbols where not visible. In **a**, symbols represent CaO content and data points are grouped by FeO_T content, as shown along the x-axis, while in panel **b**, data points are grouped by reactive gas and duration, also marked on the x-axis. Experiment temperatures for both panels are indicated by symbol outline color, as shown in the key in **a**. Note changes between the median, shown here, and the mean crystal volume in Fig. 11, particularly for Krafla experiments

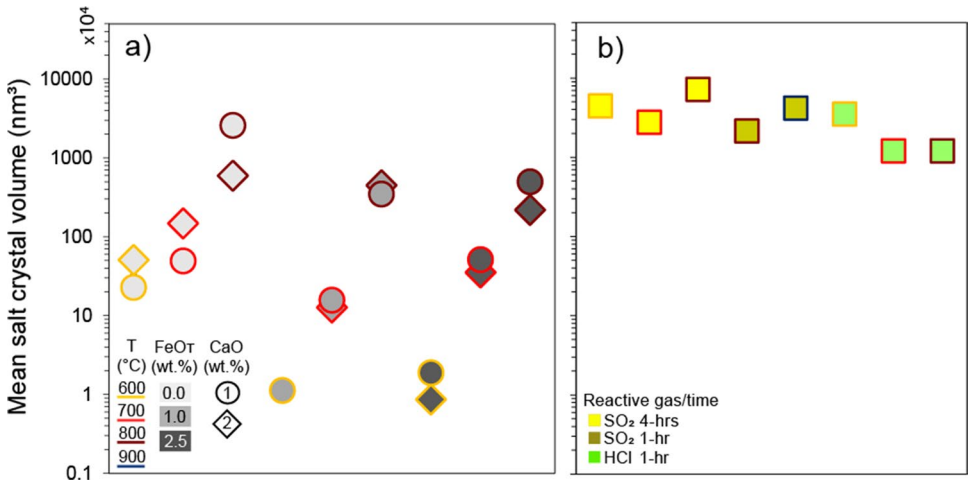

Fig. 11 Mean salt crystal volume (nm^3) obtained for **a** HPG8 and **b** Krafla treated samples. Note the increase in mean size compared to median for all data points. Some data points, such as those for salts produced during HCl experiments, have a significantly higher mean than median volume, although most relative trends between experiments remain very similar to the median data plotted in Fig. 10 and used for salt loading calculations in Fig. 13

conditions (e.g., 96 mol.% H_2O), the presence of water vapor did not significantly affect salt growth. Evidently, this study represents a step forward into the development of more quantitative investigations of ash surfaces; however, direct comparisons to natural volcanic ash deposits should be performed with caution. Syn-eruptive formation of surficial salts on ash at high temperatures ($T > > 200$ °C) has been investigated before and has been suggested to begin with adsorption of hot gas molecules onto the reactive sites of freshly fragmented glassy ash, process known as chemisorption, followed by heterogenous reactions that lead to nucleation of the first surficial salt crystals (e.g., $CaSO_4$).

This effectively results in extraction of salt-forming cations (alkalis or alkaline-earth) from the glass surface, leaving vacancies that produce a chemical gradient, triggering cation outward flux towards the particle surface to sustain further gas-glass reactions (Ayris et al. 2013; Renggli and King 2018; Delmelle et al. 2018; Casas et al. 2019). Here, we evaluated the effect of various experimental parameters (glass- and gas-mixture composition, temperature, exposure time) on the surface coverage and morphometrics of salts formed on glass particle surfaces and then compared the results with leachate data. We observed that for a set of three samples treated at $T = 800$ °C with SO_2, HPG8 (1–2 wt.% CaO and 0–2.5 wt.% FeO_T) and Krafla rhyolite (1.7 wt.% CaO and 3.26 wt.% FeO_T), the salt surface coverage remained at $64 \pm 2\%$, despite their varying composition and exposure times (0.5 h for the HPG8 samples and 1 and 4 h for Krafla rhyolite). In order to evaluate the amount of

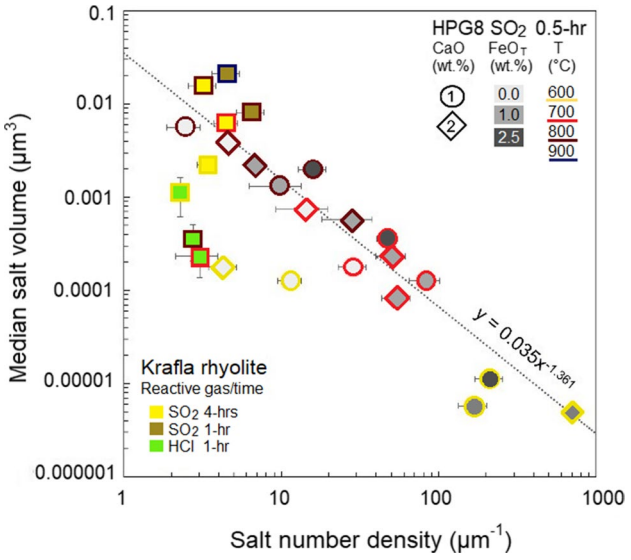

Fig. 12 Median salt volume is plotted against salt number density, with varying FeO_T content (grey shades), CaO content (symbol type), and temperature (border colors) for all HPG8 samples, and varying reactive gas and exposure time for all Krafla samples. Number density error bars show the standard error from multiple images of the same sample; where only one image was measured, the average error from all other datasets was plotted (i.e., ± 20%). Median volume error bars show the median absolute error, calculated as 1.25 × mean absolute error (MAE). The linear regression has a power law form, as shown, with R^2 of 0.77. The distribution of data for HPG8 samples appears to be grouped by temperature, but with notable anomalies for Fe-free experiments at 600 °C, which produce relatively coarse and sparse salts compared to the other 600 °C experiments

calcium extracted from these samples that is incorporated into surficial salts, we use the concept of normalized calcium (Ca/Ca_i), i.e., the ratio between the amount of leached calcium (Ca) and the bulk calcium in the glass (Ca_i), shown in Fig. 3 for all samples. When comparing the leachate data of these three samples, we observe a good agreement of normalized calcium of both HPG8 CaO 1 and CaO 2, as $Ca/Ca_i = 0.53$ and 0.46, respectively, while Krafla rhyolite had a value of 0.71, matching the relative changes in median salt volumes reported in Fig. 10.

These results provide an indication that crystal formation is limited by temperature, which may exert a more powerful control than both the reaction time or the glass composition. The temperature dependence of surficial salts formation, evidenced by leachate analysis, can be explained by the structural properties of glasses, as cation mobility in glasses is known to be enhanced at temperatures near the glass transition temperature, Tg, which marks the onset of glass relaxation, where the structure is reorganized and commences to behave more like a viscous liquid than a rigid solid (Dingwell and Webb 1989), thus enhancing cation mobility and chemical diffusivity (Zhang et al., 2010). To confirm this, Tg was measured by differential calorimetry for all samples prior to the experiments, i.e., for the six HPG8 glasses (doped with 1 and 2 wt.% of CaO and 0, 1, and 2.5 wt.% FeO_T each) and for the Krafla obsidian. For HPG8 CaO 1 glasses, Tg values showed negligible variation upon increasing FeO_T, such that for all three samples, such that Tg ~ 811.5, whereas, for HPG8 CaO 2 glasses, Tg values slightly decreased with increasing iron content as Tg = 790, 777, and 760 °C, for $FeO_T = 0$, 1, and 2.5 wt.%, respectively. Tg for the Krafla glass was measured to be 680 °C. Given the fact that all measured Tg values were within the temperature range used in our experiments (600–900 °C), we assume that the positive correlation observed between increasing temperatures and salt growth can be the result of approaching or crossing the glass transition temperature of the samples.

For instance, for Krafla samples, it was observed that decreasing experimental temperatures result in a proportional decrease of salt surface coverage (Fig. 4c and Fig. 7b) and volume (Figs. 10b and 11b), yet in the case of HPG8 experiments, variations in temperature did not always produce a regular change in coverage and volume. This might be explained by the additional effect of varying the FeO_T content in these samples. In Figs. 4a, b, 10a, and 8a, it is shown that salt coverage, salt crystal volume, and salt number density, respectively, vary in SO_2 experiments according not only to temperature but also to the glass composition, which indirectly controls cation mobility. The most unexpected result observed here was effect of varying CaO content in each set of HPG8 samples. Addition of calcium was thought to be the compositional parameter that would exert the strongest control on the abundance and size of surficial salt formation, due to the ubiquity of calcium in surficial salts found in nature (Witham et al. 2005) and through experimental work (Ayris et al. 2013; Renggli and King 2018; Casas et al. 2019). Yet it was evident here that FeO_T rather than CaO content was exerting the most significant compositional control on salt formation and morphology. The role of iron in volcanic glass on the formation of surficial salts during gas-ash reactions, in particular on cation diffusion, is still not fully understood.

The difficulties in constraining the dynamics and mechanisms of iron oxidation arise from the influence of multiple factors: the initial glass redox state (Mysen and Richet 2005); bulk composition, i.e., the presence of other multivalent cations in the glass network (Farges et al. 2004); chemistry and redox nature of the gas (King et al. 2018); and temperature (Mysen and Virgo 1984). Nevertheless, some studies have looked into the compositional changes of Fe-bearing glasses upon high-temperature exposure to SO_2 gas and have observed changes in the redox state of treated samples—namely, that these become more oxidized upon reactions with gases, i.e., during surficial salt formation (Renggli and King, 2018; Renggli et al. 2019). The acting mechanism for iron oxidation has been proposed to be the

diffusive removal of network modifying cations (e.g., Ca^{2+} and Mg^{2+}), triggered by surficial crystal formation, which causes an internal electrochemical potential, that requires charge compensation by changing the redox state of polyvalent cations (in this case Fe^{2+}/Fe^{3+}). This was suggested by Cook et al. (1990) and Cooper et al. (1996) after results of their oxidation experiments of H-free basaltic glasses in air at high temperatures (550–600 °C), resulted in formation of a thin coating of alkaline earth metal oxides, CaO or MgO, as well as an increase in their Fe^{3+}/Fe_T ratio, thus iron oxidation. As our SO_2-glass experiments also produced changes in the bulk Fe-redox state of samples that were proportional to the amount of calcium mobilized from the bulk glass to the free surface to form $CaSO_4$ (see Supplementary Fig. 4), it is reasonable to infer that analogous redox-diffusion dynamics took place for both Krafla and HPG8 samples.

Furthermore, the fact that increasing calcium oxide content in HPG8 glasses (from 1 to 2 wt.% CaO), produced similar results of the total amount, distribution, and crystal volume of salts (Figs. 3, 4, and 10), indicates that formation of Ca-bearing salts by means of high-temperature glass-gas (SO_2, HCl) reactions, does not appear to be limited by the availability of bulk calcium in glass. If so, we would have observed a higher salt content in CaO 2 samples than in the CaO 1 glasses, under the same experimental conditions. As this was not the case, there must be another parameter limiting salt formation, such that any calcium "excess" becomes negligible for Ca-bearing salt formation in glasses. The striking similarities between the total fraction of calcium extracted from the bulk glass (Ca/Cai) and the salt coverage (%) of samples HPG8 CaO 1 and CaO 2 showed in Figs. 3a, b and 4a, b, respectively, suggest that, regardless of the composition and reaction temperatures, salt-formation control might be ultimately limited by the availability of surficial reactive sites for gas molecules to adsorb onto and react with glass. We propose that, once the surface reaches a saturation point, where free glass surface is not accessible to gas molecules, both chemisorption and calcium diffusion, regardless of the composition, are expected to decrease. Our argument can be further be supported by comparing the salt coverage obtained by HPG8 glasses with those of Krafla rhyolite.

In Fig. 4a–c, we see that the maximum surface coverage of all samples ranges between 66 and 72%, despite the differences in treatments and compositions; a coverage of 66% was obtained by the HPG8 sample doped with 1 wt.% CaO and 2.5 wt.% FeO_T and treated for 0.5 h, while 64 and 65% of coverage were obtained by the Krafla rhyolite (1.6 wt.% CaO and 3.26 wt.% FeO_T) treated for 1 and 4 h, respectively, both at 800 °C under SO_2-Ar atmospheres. Despite the reaction times being two to eight times longer for the latter, the surface coverage does not increase with respect to the first. We therefore propose that, while calcium in the bulk glass is needed to nucleate and sustain salt growth upon glass-gas reactions, the availability of reaction surface sites is perhaps the key control of ash-gas reactions. Formation of surficial salts on Fe-free HPG8 samples, evidenced by leachates analysis and SEM images, indicates that this cation outward diffusion occurred also in the absence of iron. The mechanism which took place to balance the internal charge changes left by cation surface migration in this case is yet to be comprehended. However, it has been proposed that, in glasses exposed at high temperatures, the absence of polyvalent species able to change their redox state to accommodate internal electrochemical potential, diffusion of Ca^{2+} cations occurs by co-diffusion with singly bonded oxygens (Sucov and Gorman 1969).

Studies of tracer diffusion have shown that Ca^{2+} mobility is enhanced by the presence of alkaline ions of similar ionic radius, i.e., Na^+, if $r_{Ca^{2+}}/r_{Na^+} \approx 1$. When this occurs in soda-lime silicate glasses, the activation energy of calcium diffusion displayed its minimum values (e.g., Natrup et al. 2002, 2005). While more experimental work is needed to fully establish mechanism(s) of cation diffusion in Fe-free glasses, it was clear from this work that the presence of iron influences both the amount of surficial salts leached and their size. For instance, it is interesting that the size of salt crystals formed in Fe-free experiments is larger than those in Fe-bearing experiments (Fig. 5). This suggests that crystal growth dominated over nucleation, which might reflect the change in Ca-diffusion mechanisms. Figures 8a, 10a, and 12 exhibit that, at any given temperature, variations in the iron content influence both the salt volume and salt number density. Increasing FeO_T is consistent with higher salt number density, suggesting an increase in nucleation sites for salt. Consistently decreasing salt number density with temperature may be due to either (i) rapid growth rates depleting Ca in a larger volume around the crystal nucleus and inhibiting further nucleation or (ii) merging and assimilation of incipient crystals into a growing structure. Assimilation of crystals during growth appears to be indicated by the decrease in salt number density and increase in volume (Fig. 12) between 1- and 4-h experiments on Krafla obsidian at 800 °C.

Interestingly, the Fe-free HPG8 samples treated at 600 °C (i.e., under the glass transition temperature), do not match the trend of all other experiments for salt number density, supporting a change in the limiting mechanism for Ca diffusion; the salts formed under these conditions were also relatively large compared to those with higher Fe content, perhaps due the lack of Ca depletion from neighboring crystal growth, leading to smaller diffusion length scales and higher availability of Ca across the duration of the experiment. A good correlation is observed between median salt volume and mean salt density for all SO_2 experiments as shown by the linear regression in Fig. 12 (taking a power law form—evident by the linear distribution of data in log–log space over four orders of magnitude—with R^2 of 0.77), suggesting

a simple trade-off between salt growth and number density (at least when the diffusion mechanism remains constant: data points for both Fe-free experiments at 600 °C are anomalous). In order to better compare the Ca^{2+} leachate (used as a proxy for surficial salt abundance) and image analysis results, we calculate the salt surface loading. We use the calculated salt crystal volumes to estimate salt loading for each experiment, by dividing the sum of median salt volumes by the sum of measured area (i.e., total measured surface area that is not occupied by non-salt particles, defined as "canvas area" in the macro) in all analyzed SEM images for that experiment. This provided a value for average salt volume (μm^3) per unit area (μm^2) on the glassy ash analogs.

For some modeling scenarios, this can be conveniently approximated to an equivalent salt thickness across the entire particle surface. We plot the results in Fig. 13 and observe, in general, a very good correlation with the leaching results in Fig. 3, with a couple of exceptions: certain features, such as the higher Ca^{2+} leachate at 600 °C of Krafla samples are not well reproduced, and values for CaO 2 experiments appear slightly lower than indicated in Fig. 3 (bearing in mind that CaO 2 samples have twice the initial CaO content; therefore, Ca/Ca_i bears twice the total Ca for the same value). As a final step, we directly assess the correlation between image analysis and leachate results by estimating the total Ca mass fraction per sample from image analysis and analytical results. Ca mass fraction was obtained using the salt loading and the specific surface area of each sample (Supplementary Table 1), under the assumption that, in anhydrous conditions, all salts were anhydrite. We calculate Ca estimated from image analysis vs the initial Ca (i.e., Ca/Ca_i) in each sample and plot them directly against the data from leachate analysis (Fig. 14). This shows good correlation for the HPG8 samples, but a significant overestimation of total Ca for the Krafla samples. The overestimation is most likely caused by error in the volume calculation, with Krafla salts showing an apparent lower profile to the HPG8 salts (Fig. 10).

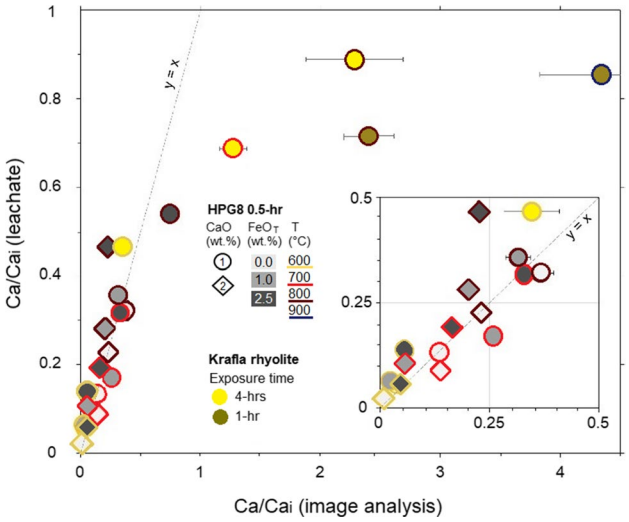

Fig. 14 Normalized calcium concentration (Ca/Ca_i) derived from leachate, specific surface area, and image analysis results are compared. The data at lower Ca/Ca_i values is magnified in the inset for clarity. Error bars show the mean absolute error and are smaller than the symbols where not shown. Good correlation is found for results from HPG8 experiments, as indicated by clustering around the y = x line. Above 600 °C, the correlation becomes increasingly poor for experiments on Krafla samples, with the image analysis method overestimating Ca by up to 4–5 times the initial Ca present in the glass

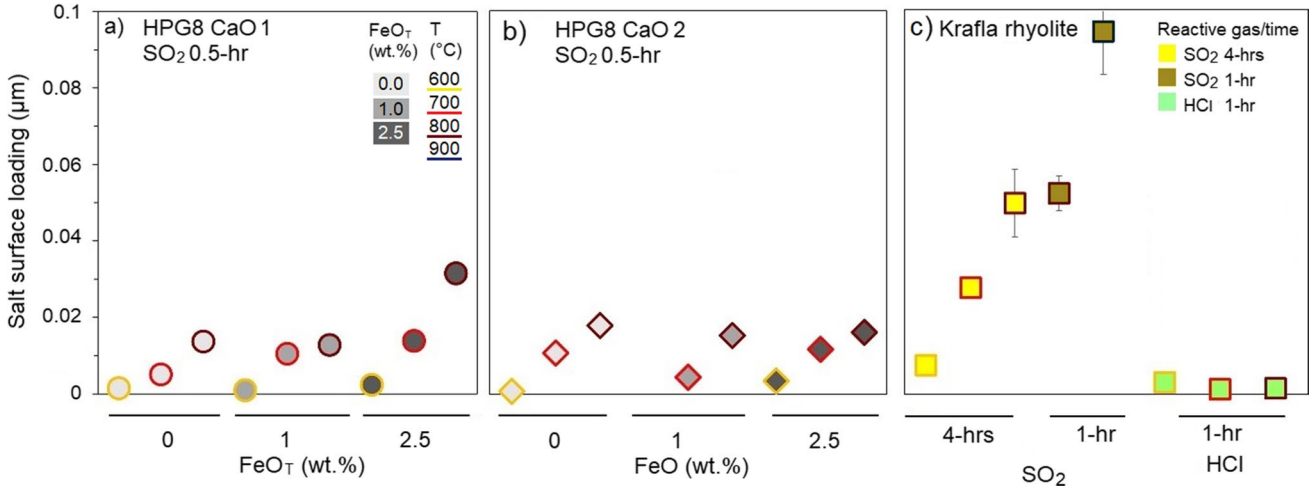

Fig. 13 Estimated salt loading (the total volume of salts per square micron of particle surface) is plotted for all HPG8 and anhydrous Krafla experiments. The sum of salt volumes from images for each experiment was divided by the sum of measured image areas to obtain the average salt surface loading. This can be considered as an equivalent salt thickness across the entire ash surface. The temperature legend in **a** also applies to panels **b** and **c**

Use of a cuboid model to estimate salt volume is simplistic, and more realistic shapes will likely improve volume estimates considerably. However, the good correlation observed for all HPG8 samples across a range of compositional and temperature variations is encouraging and suggests that image analysis can provide an accurate and estimation of salt concentrations and loading, in addition to a set of complementary morphometric information that can help to elucidate salt formation processes during high-temperature ash-gas reactions. As we observed distinct crystal shapes that were strongly dependent on the gas mixture, temperature, and glass composition, we pose that our method could eventually be used to decipher the formation conditions of salts on ash. However, this evidently will require a broader dataset of samples—ideally volcanic ash from various volcanoes, geographic settings, ages, etc.—as well as further experimental work. Normalized calcium concentrations display a consistent increase upon higher temperatures and FeO_T content, apparently regardless of the total CaO content, as fairly similar results of calcium leachate concentrations were obtained for samples HPG8 CaO 1 and CaO 2. When comparing the relative variability observed for salt surface coverage, salt crystal volume, and the effects of FeO_T content and temperature of HPG8 CaO 1, and CaO 2 samples with leachate information, it becomes clear that the bulk chemical information obtained from leachates does not necessarily represent the abundance (surface coverage) and size (crystal area) of the salts on ash surfaces.

Krafla rhyolite samples treated with SO_2 for 4 h produced the highest salt surface coverage and crystal volumes from all samples for each treatment temperature; similarly, the highest calcium concentrations were obtained for these samples, being the sample treated at 800 °C (Fig. 4c) capable of extracting a fraction of 0.88 of the glass bulk calcium. Results of the SEM images analysis of Krafla rhyolite treated under HCl-atmospheres (all for 1 h long), shown in Fig. 5c, display good agreement with the leachate data (Fig. 4c), as in the case of SO_2-treated samples, i.e., high salt surface coverage (%) and salt crystal area values corresponded to high Ca/Ca_i values. These results differ, however, from those of SO_2 experiments; for instance, temperature dependence of Ca/Ca_i concentrations displays an opposite relationship, i.e., increasing temperatures seem to reduce Ca/Ca_i values and also, for all temperatures, concentrations of leached calcium, are lower than those of SO_2-treated samples. The mechanism by which surficial salts form under HCl atmospheres has been proposed to be by inward migration of protons, H^+, from HCl, supported by outward migration of mono- or divalent-cations (Douglas et al. 1949; Koenderink et al. 2000). The pathway for this mechanism has been observed by Elmer (1981) to be hindered by surface dehydroxilisation, at $T \sim 600$–800 °C, in agreement with our results.

Conclusions

Using a SEM-based semi-automatized method, we have quantified for the first time the morphometrics of surficial salts on volcanic ash proxies. Our methodology proved to be successful in distinguishing salts from particle–surface areas, and in quantifying relevant salt properties, such as the surface coverage, area, volume, salt loading, number density, and roundness of surficial salt crystals. The good agreement observed between the salt morphometrics and leachate data demonstrates the suitability of our methodology to investigate salt-formation processes. Furthermore, results of our high-temperature SO_2-glass experiments, in particular of the set of HPG8 glasses, showed almost negligible variations of both the amount of calcium extracted from the glass to form surficial slats (assessed by leachate analysis) and the salt-morphometrics, upon changing the bulk calcium content (wt.% CaO). In contrast, varying the total iron content of glasses, from 0 to 2.5 wt.% FeO_T, resulted in noticeable morphological changes of the salts: HPG8 Fe-free and Fe-low (i.e., 0 and 1 wt.% FeO_T) glasses produced fewer, more elongated crystals, while Fe-rich samples, HPG8 2.5 wt.%FeO_T and Krafla rhyolite (3.26 wt.%FeO_T), consistently produced more and blockier crystals. This implies that, from a compositional point of view, iron appears to exercise a more dominant control on salt formation (influencing salt nucleation, growth, or both), than previously thought.

Moreover, the novel observations made here, regarding the positive correlation between increasing oxidation of iron and increasing temperatures, both coupled with enhanced salt formation in all Fe-bearing salts, suggest that iron oxidation might ultimately be the driving force for SO_2 uptake by glass. Additionally, results of salt surface coverage (%) showed that, regardless of the composition, temperature, or exposure time, salt formation is more strongly controlled by the availability of salt nucleation sites, rather than availability of bulk calcium in the glass. Nonetheless, the effect of reaction time did influence the salt shape and size, being salt crystals coarser after 4 h exposure to SO_2 exposures, than after 0.5 h. Collectively, our results showed the advantages of coupling experimental work with chemical analysis (leachates and redox-sate determinations) and with the protocol presented here to investigate salt formation processes resulting from solid–gas interactions. Further research that combines morphometric analysis of salts with experimental work could be conducted to help determine nucleation, growth, and dissolution rates of salts, structural arrangement,

volume, and textural changes of the solid surface, as well as help the development of crystallization models under diverse reaction conditions. In addition, the mechanisms of particle surface-mediated atmospheric processes such as cloud and ice nucleation could be better comprehended by improving the quantitative characterization of ash surfaces and ice and water nuclei under controlled experimental conditions. Finally, we propose that SEM-based morphometric analysis is underexploited in geosciences and can become a reliable and accessible source of information regarding many other surface processes, such as annealing, sintering, melting, and general crystallization processes of solid geological specimens (rocks, minerals, aggregates, glasses, soil, etc.), and therefore, we encourage Earth scientists to (re)consider the potential of morphometric microcharacterization into their research.

Supplementary Information The online version contains supplementary material available at https://doi.org/10.1007/s00445-021-01519-3.

Acknowledgements We thank Kai-Uwe Hess for conducting the Tg measurements and Antonia Wimmer for analytical assistance. We are grateful to Fabian B. Wadsworth for providing Krafla rhyolite material. We express our gratitude to two anonymous reviewers and to the editor for providing constructive comments and suggestions that helped us improve the quality of our manuscript.

Funding Open Access funding enabled and organized by Projekt DEAL. ASC was funded by the Mexican council of science and technology and by the German academic exchange service with the Ph.D. studentship grant CONACyT-DAAD Nr. 409903. AH acknowledges funding from the European Union via a Marie Curie Fellowship (AVAST 653900) and a NASA IDS grant "Volcanic Ash and Its Impacts the Earth System" (19-IDS19-0083). DBD acknowledges support from the European Research Council via the Advanced Grant 2018 no. 834225 (EAVESDROP) and the AXA Research Grant "Risk from volcanic ash in the earth system."

References

Armienta MA, Martin-Del-Pozzo AL, Espinasa R, Cruz O, Ceniceros N, Aguayo A, Butron MA (1998) Geochemistry of ash leachates during the 1994–1996 activity of Popocatépetl volcano. Appl Geochem 13(7):841–850

Ayris PM, Delmelle P (2012) The immediate environmental effects of tephra emission. Bull Volcanol 74(9):1905–1936

Ayris PM, Lee AF, Wilson K, Kueppers U, Dingwell DB, Delmelle P (2013) SO_2 sequestration in large volcanic eruptions: high-temperature scavenging by tephra. Geochim Cosmochim Acta 110:58–69

Ayris PM, Delmelle P, Cimarelli C, Maters EC, Suzuki YJ, Dingwell DB (2014) HCl uptake by volcanic ash in the high temperature eruption plume: mechanistic insights. Geochim Cosmochim Acta 144:188–201

Ayris PM, Cimarelli C, Delmelle P, Wadsworth FB, Suzuki VJ, YJ, Dingwell DB, (2015) A novel apparatus for the simulation of eruptive gas-rock interactions. Bull Volcanol 77:104

Banks N, Hoblitt R (1981) Summary of temperature studies of 1980 deposits. The 1980 eruptions of Mount St. Helens US Geol Surv Prof Pap 1250:295–313

Brunauer S, Emmett PH, Teller E (1938) Adsorption of gases in multimolecular layers. J Am Chem Soc 60(2):309–319

Casas AS, Wadsworth FB, Ayris PM, Delmelle P, Vasseur J, Cimarelli C, Dingwell DB (2019) SO_2 scrubbing during percolation through rhyolitic volcanic domes. Geochim Cosmochim Acta 257:150–162

Castro J, Dingwell D (2009) Rapid ascent of rhyolitic magma at Chaitén volcano, Chile. Nature 461:780–783

Cook GB, Cooper RF, Wu T (1990) Chemical diffusion and crystalline nucleation during oxidation of ferrous iron-bearing magnesium aluminosilicate glass. J Non-Cryst Solids 120(1–3):207–222

Cooper RF, Fanselow JB, Poker DB (1996) The mechanism of oxidation of a basaltic glass: chemical diffusion of network-modifying cations. Geochim Cosmochim Acta 60(17):3253–3265

Darbon J, Cunha A, Chan T, Osher S, Jensen G (2008) Fast nonlocal filtering applied to electron cryomicroscopy. 5th IEEE International Symposium on Biomedical Imaging: From Nano to Macro, Proceedings, ISBI. 1331–1334. https://doi.org/10.1109/ISBI.2008.4541250

Delmelle P, Wadsworth FB, Maters EC, Ayris PM (2018) High temperature reactions between gases and ash particles in volcanic eruption plumes. Rev Mineral Geochem 84(1):285–308

Dingwell DB, Webb SL (1989) Structural relaxation in silicate melts and non-Newtonian melt rheology in igneous processes. Phys Chem Miner 16:508–516

Douglas RW, Isard JO (1949) The action of water and of sulphur dioxide on glass surfaces. J Soc Glass Technol 33:289–335

Elmer TH (1981) Dehydroxylation of porous glass by means of chlorine. J Am Ceram Soc 64(3):150–154

Farges F, Lefrère Y, Rossano S, Berthereau A, Calas G, Brown GE (2004) The effect of redox state on the local structural environment of iron in silicate glasses: a combined XAFS spectroscopy, molecular dynamics, and bond valence study. J Non-Cryst Solids 344:176–188

Guimarães L, Hornby A, Kueppers U, Alves A, Janasi V, Dingwell D (2019) Generation of block-and-ash flows at the onset of silicic volcanism in the Paraná Magmatic Province (Brazil): evidence from photoanalysis of Caxias do Sul breccias. Bull Volcanol 81. https://doi.org/10.1007/s00445-019-1332-7

Heiken GH (1972) Morphology and petrography of volcanic ashes. Geol Soc Am Bull 83:1961–1988

Heiken GH (1974) An atlas of volcanic ash. Smithsonian Contrib Earth Sci 12:1–101

Heiken G, Wohletz K (1985) Volcanic ash. University of California Press, Sharp and Simmons, p 246

Holtz F, Behrens H, Dingwell DB, Taylor RP (1992) Water solubility in aluminosilicate melts of haplogranitic compositions at 2 kbar. Chem Geol 96:289–302

Hornby A, Kueppers U, Mauer B, Poetsch C, Dingwell DB (2020) Experimental constraints on volcanic ash generation and clast

morphometrics in pyroclastic density currents and granular flows. Volcanica 3(2):263–283
King PL, Wheeler VW, Renggli CJ, Palm AB, Wilson SA, Harrison AL, Morgan B, Nekvasil H, Troitzsch U, Mernagh TP, Yue L, Bayon A, DiFrancesco NJ, Baile R, Kreider P, Lipiński W (2018) Experimental approaches and theoretical aspects of gas-solid reactions with case studies. Rev Mineral Geochem 84:1–56
Koenderink GH, Brzesowsky RH, Balkenende AR (2000) Effect of the initial stages of leaching on the surface of alkaline earth sodium silicate glasses. J Non-Cryst Solids 262(1):80–98
Le Maitre RW, Streckeisen A, Zanettin B, BasMJ Le, Bonin B, Bateman P, Bellieni G, Dudek A, Efremova S, Keller J, Lamere J, Sabine PA, Schmid R, Sorensen H, Woolley AR (2002) Igneous rocks: a classification and glossary of terms, recommendations of the International Union of Geological Sciences Subcommission of the Systematics of Igneous Rocks. Cambridge University Press, Cambridge, p 256
Legland D, Arganda-Carreras I, Andrey P (2016) MorphoLibJ: Integrated library and plugins for mathematical morphology with ImageJ. Bioinformatics 32:3532–3534
Liu EJ, Cashman KV, Rust AC (2015) Optimising shape analysis to quantify volcanic ash morphology. GeoResJ 8:14–30
Münch B, Gasser P, Holzer L, Flatt R (2006) FIB nanotomography of particulate systems - Part II: Particle recognition and effect of boundary truncation. J Am Ceram Soc 89(8):2586–2595
Mysen BO, Virgo D, Seifert F (1984) Redox equilibria of iron in alkaline earth silicate melts: relationships between melt structure, oxygen fugacity, temperature and properties of iron-bearing silicate liquids. Am Mineral 69:834–847
Mysen BO, Richet P (2005) Silicate glasses and melts: properties and structure. Elsevier, Amsterdam, Boston
Natrup F, Bracht H, Martiny C, Murugavel S, Roling B (2002) Diffusion of calcium and barium in alkali alkaline-earth silicate glasses. Phys Chem Chem Phys 4:3225–3231
Natrup FV, Bracht H, Murugavel S, Roling B (2005) Cation diffusion and ionic conductivity in soda-lime silicate glasses. Phys Chem Chem Phys 7:2279–2286
Óskarsson N (1980) The interaction between volcanic gases and soild tephra. J Volcanol Geotherm Res 8:251–266
Paterson G, Roberts A, Mac Niocaill C, Muxworthy A, Gurioli L, Viramonte J, Navarro C, Weider S (2010) Paleomagnetic determination of emplacement temperatures of pyroclastic deposits: an under-utilized tool. Bull Volcanol 72:309–330
Pyle D (2000) Sizes of volcanic eruptions. In: Sigurdsson H, Houghton B, McNutt S, Rymer H, Stix J (eds) Encyclopedia of Volcanoes. Academic Press, London, pp 263–269
Rampino MR, Self S (1982) Historic eruptions of Tambora (1815), Krakatau (1883), and Agung (1963), their stratospheric aerosols, and climatic impact. Qua Res 18:127–143
Renggli CJ, King PL (2018) SO_2 gas reactions with silicate glasses. Rev Mineral Geochem 84(1):229–255
Renggli CJ, Palm AB, King PL, Guagliardo P (2019) Implications of reactions between SO2 and basaltic glasses for the mineralogy of planetary crusts. J Geophys Res Planets 124:2563–2582
Rogers N, Hawkesworth C (2000) Composition of magma. In: Sigurdsson H, Houghton B, McNutt S, Rymer H, Stix J (eds) Encyclopedia of Volcanoes. Academic Press, London, pp 115–131
Rose WI, Bonis S, Stoiber RE, Keller M, Bickford T (1973) Studies of volcanic ash from two recent Central American eruptions. Bull Volcanol 37(3):338–364
Rose WI (1977) Scavenging of volcanic aerosol by ash: Atmospheric and volcanologic implications. Geology 5(10):621–624
Rose WI, Durant AJ (2009) Fine ash content of explosive eruptions. J Volcanol Geotherm Res 186(1–2):32–39
Schneider CA, Rasband WS, Eliceiri KW (2012) NIH Image to ImageJ: 25 years of image analysis. Nat Methods 9(7):671–675
Shapiro L, Brannock WW (1956) Rapid analysis of silicate rocks. U.S. Geol Surv Bull 1036C:32–34
Sparks RSJ (1986) The dimensions and dynamics of volcanic eruption columns. Bull Volcanol 48:3–15
Sucov EW, Gorman RR (1969) Interdiffusion of calcium in soda-lime-silica glass at 880 °C to 1308 °C. J Am Ceram Soc 48:426–429
Taylor PS, Stoiber RE (1973) Soluble material on ash from active Central American volcanoes. Geol Soc Am Bull 84(3):1031–1042
Textor C, Graf HF, Timmreck C, Robock A (2003) Emissions from volcanoes. In: Granier C, Reeves C, Artaxo P (eds) Emissions of chemical compounds and aerosols in the atmosphere. Kluwer Publishers, Dordrecht, pp 269–303
Tuffen H, Castro JM (2009) The emplacement of an obsidian dyke through thin ice: Hrafntinnuhryggur. Krafla Iceland J Volcanol Geotherm Res 185(4):352–366
Wagner T, Lipinski H (2013) IJBlob: an ImageJ library for connected component analysis and shape analysis. J Open Res Softw 1(1):6–8
Wilson TM, Stewart C (2012) Volcanic ash. In P, Bobrowsky (ed.). Encyclopaedia of Natural Hazards. Springer. p. 1000
Witham CS, Oppenheimer C, Horwell CJ (2005) Volcanic ash-leachates: a review and recommendations for sampling methods. J Volcanol Geotherm Res 141(3–4):299–326
Zhang Y, Ni H, Chen Y (2010) Diffusion data in silicate melts. Rev Mineral Geochem 72:311–408